Supplementary Information (SI) for ChemComm.
This journal is © The Royal Society of Chemistry 2026

Facet-Engineered Prussian Blue Analog Nanosheet-Assembled Superstructures for Efficient Syngas Production

Quan Zhou,†[a] Shuai Li,†[a] Zixuan Li,[a] Shibao Liu,[a] Fan Gu,[a] Binghui Yu,[a] Qiangqiang Qiao,[a] Yujing Liu,[a] Huadong Yuan,[a] Jianmin Luo,[a] Yao Wang,[a] Shihui Zou,[a] Peng Shi,[b] Xinyong Tao[a], Jianwei Nai*[a]

a. College of Materials Science and Engineering, Zhejiang University of Technology, Hangzhou 310014, China. E-mail: jwnai@zjut.edu.cn
b. Science and Education Integration College of Energy and Carbon Neutralization, Zhejiang University of Technology, Hangzhou 310014, China

† These authors contributed equally to this work.

S1. Experimental

1.1 Materials

All experimental materials and reagents used in this study are listed as follows：

Copper(II) nitrate trihydrate ($Cu(NO_3)_2·3H_2O$, 99%, Macklin), trimesic acid ($C_9H_6O_6$, 99%, Aladdin), lauric acid ($C_{12}H_{24}O_2$, 99%, Adamas), sodium citrate dihydrate ($C_6H_5Na_3O_7·2H_2O$, 99%, Sigma-Aldrich), tripotassium hexacyanocobaltate (III) ($K_3Co(CN)_6$, 98%, Aladdin), 1-butanol ($C_4H_{10}O$, 99.5%, Sinopharm), 1,3-dimethyl-2-phenyl-2,3-dihydro-1H-benzo[d]imidazole (BIH, 97%, Aladdin), Triethanolamine (TEOA, 99%, Aladdin), tris (2,2'-bipyridyl) dichlororuthenium (II) hexahydrate ($[Ru(bpy)_3]Cl_2·6H_2O$, 99.95%, Aladdin), acetonitrile (CH_3CN, 99.9%, Aladdin), ultrapure water (UP water, 18 MΩ·cm), ethanol (C_2H_5OH, 99.8%, Aladdin), ultra-high-purity CO_2 (99.999%) were used without any further treatment.

1.2 Preparation of HKUST-1 nanocubes

The HKUST-1 nanocubes were synthesized by referring to a previous report.[1] Dissolve 123 mg of $Cu(NO_3)_2·3H_2O$, 72 mg of trimesic acid, and 12.75 g of lauric acid in 45 mL of 1-butanol, and stir until completely dissolved. The resulting solution was transferred to a 100 mL Teflon-lined stainless steel auto-clave and reacted at 120 °C for 6 hours. The precipitate was collected by centrifugation, washed three times with ethanol, and dried at 70 °C for 6 hours to obtain HKUST-1 nanocubes.

1.3 Preparation of H-CuCo PBA

H-CuCo PBA was synthesized via an anion exchange strategy. 25 mg of HKUST-1 was dispersed in a mixed solution of 12.5 mL of ethanol and 2.5 mL of UP water and magnetically stirred for 1 h to pre-activate the material. Subsequently, 20 mL of cobalt potassium cyanide aqueous solution (concentration of 5 mg ml^{-1}) was added, and the reaction was continued for another 3 h. The resulting product was collected by centrifugation, washed sequentially with water and ethanol, and then dried overnight for subsequent use.

1.4 Preparation of C-CuCo PBA

C-CuCo PBA was synthesized via a coprecipitation method at room temperature. Solution A was prepared by dissolving 289 mg of cupric nitrate trihydrate and 500 mg of sodium citrate dihydrate in 30 mL of ultrapure water. Solution B was prepared by

dissolving 266 mg of potassium cobalt cyanide in 30 mL of ultrapure water. After complete dissolution of both solutions, solution B was added dropwise into solution A under magnetic stirring for 10 min. The resulting mixture was then left to age for 3 h. The obtained C-CuCo PBA product was collected by centrifugation, washed sequentially with water and ethanol, and finally dried at 70 °C overnight.

1.5 Materials characterization

The X-ray diffraction (XRD) patterns of the sample were characterized using an X-ray diffractometer (Bruker, D2 Phasertong Cu Kα). The morphology and microstructure of the obtained samples were characterized using field-emission scanning electron microscopy (FESEM, Nova NanoSEM 450) and transmission electron microscopy (TEM, FEI Talos-S). The elemental composition was analyzed by energy-dispersive X-ray spectroscopy (EDS) attached to the FESEM. Additionally, elemental mapping was performed using a TEM equipped with EDX spectroscopy. Fourier transform infrared spectroscopy (FT-IR) spectra were collected using KBr on an FT-IR spectrometer (V80, Bruker Corporation) and the X-ray photoelectron spectroscopy (XPS) was carried out on an energy spectrometer (Kratos AXIS Ultra DLD). Ultraviolet–visible (UV–Vis) reflectance spectra were acquired on a Shimadzu UV-3600i Plus spectrophotometer in the wavelength range of 250–800 nm. Isotopic labeling control experiments were obtained on gas chromatography-mass spectrometry (8890/7000D, Agilent Technologies).

1.6 Photoelectrochemical tests

Photoelectrochemical measurements were performed on a CHI 760E electrochemical workstation using a standard three-electrode system with 0.2 M Na_2SO_4 solution as the electrolyte. A saturated Ag/AgCl electrode was used as the reference electrode, a platinum electrode as the counter electrode, and fluorine-doped tin oxide (FTO) conductive glass as the working electrode. 2 mg of the sample was dispersed in a mixture of 350 μL of ethanol, 140 μL of ultrapure water, and 10 μL of 5% Nafion solution under ultrasonication for 30 min. Subsequently, 20 μL of the resulting dispersion was drop-cast onto a 1 cm × 1 cm FTO substrate and dried at room temperature. Mott–Schottky plots were measured at frequencies of 1000, 2000, and 3000 Hz. Electrochemical impedance spectroscopy (EIS) was recorded in the frequency range of 0.1 to 10^5 Hz with an amplitude of 5 mV. For the photocurrent response

measurements, a certain amount of $[Ru(bpy)_3]Cl_2 \cdot 6H_2O$ was dissolved in Na_2SO_4 aqueous solution as the electrolyte. A 300 W Xe lamp equipped with a UV-cutoff filter ($\lambda > 420$ nm) was used as the light source.

1.7 CO_2 photoreduction performance

Photocatalytic reactions were conducted in a 50 mL sealed quartz reaction vessel under a CO_2 atmosphere at 1 atm. The reaction system consisted of 1 mg of catalyst, 10 mg of $[Ru(bpy)_3]Cl_2 \cdot 6H_2O$, 50 mg of BIH, 10 mL of CH_3CN, and 2 mL of H_2O, with continuous magnetic stirring. Light irradiation was provided by a 300 W Xe lamp equipped with a 420 nm long-pass cutoff filter ($\lambda > 420$ nm). The gaseous products generated from the reaction were analyzed using a gas chromatograph (GC, Fuli Instruments F80) equipped with a thermal conductivity detector (TCD) and a flame ionization detector (FID).

1.8 In-situ DRIFTS measurements

In-situ DRIFTS measurements was performed using a custom-designed top-plate reaction cell with a ZnSe crystal as the infrared transmission window (cut-off energy of ~625 cm^{-1}). The end station was equipped with a Bruker 66 v/s FT-IR spectrometer coupled with a Bruker Hyperion 3000 infrared microscope (×16 objective) and a liquid nitrogen cooled mercury cadmium telluride (MCT) detector, providing a spectral range of 15–4000 cm^{-1} and a spectral resolution of 0.25 cm^{-1}. CO_2 was introduced into the cell, which was loaded with a powder mixture of $[Ru(bpy)_3]Cl_2 \cdot 6H_2O$, BIH, and H-CuCo PBA. The sample was purged with CO_2 for 30 min until its spectrum in the dark stabilized. Visible light irradiation ($\lambda > 420$ nm) was applied to the sample through a quartz window, and spectra were recorded over time to monitor the evolution of surface-adsorbed intermediates. Each spectrum was obtained by averaging 514 scans at a resolution of 2 cm^{-1}. The background spectrum was collected before light irradiation. By analyzing the appearance and evolution of characteristic vibrational peaks, key reaction intermediates (e.g., *COOH, *CO, carbonate species) were identified, elucidating the synergistic reaction pathway for CO_2 reduction to CO.

1.9 DFT calculation

All density functional theory (DFT) calculations were performed using the Vienna

Ab-initio Simulation Package (VASP).[2] The projected augmented wave (PAW)[3] method was employed within the generalized gradient approximation (GGA)[4] using the Perdew-Burke-Emzerhof (PBE)[5] exchange-correlation functional. To account for long-range dispersion-interactions, the DFT-D3 correction method of Grimme was applied. A plane-wave energy cutoff of 450 eV was used for all calculations, ensuring sufficient convergence.The Brillouin zone sampling was performed using a 5x2x1 Monkhorst-Pack k-point mesh. The electronic self-consistent field (SCF) convergence threshold was set to 10^{-5} eV, while the atomic forces were relaxed below 10^{-2} eV/Å to ensure structural optimization accuracy. A vacuum region of 15 Å was introduced along the c-axis to prevent spurious interactions between periodic images.

S2. Supplemental figures

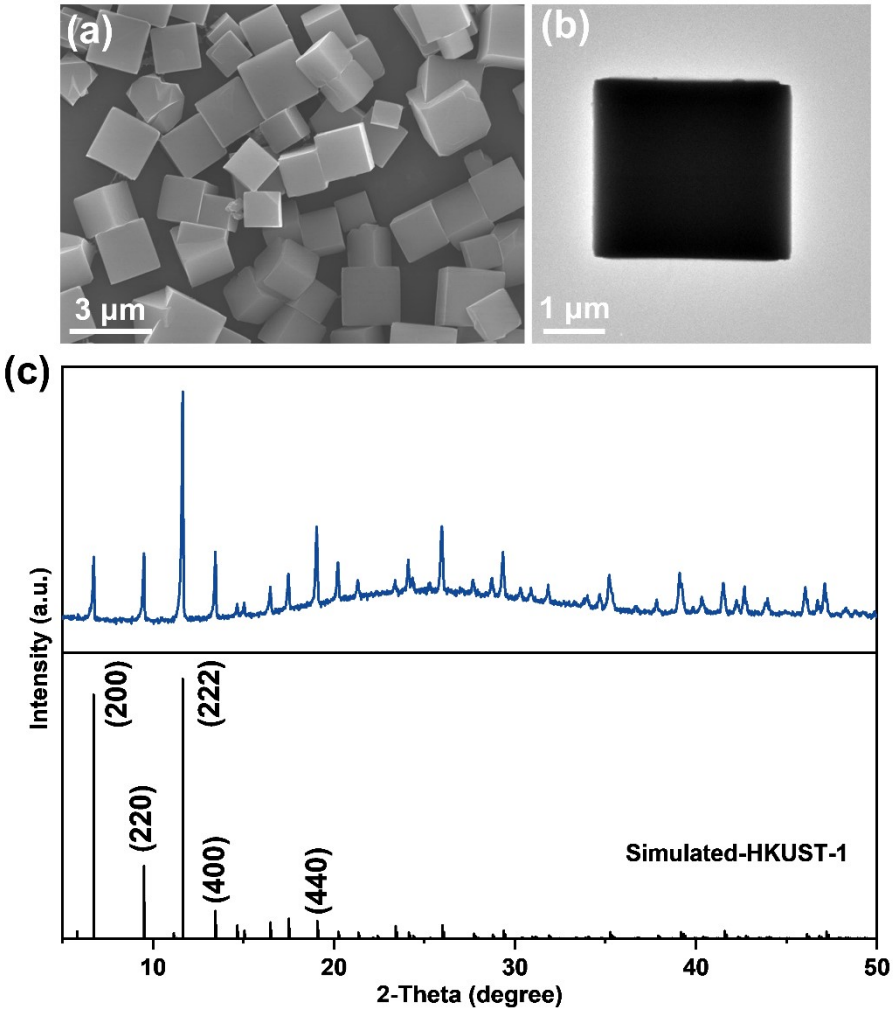

Fig. S1 (a) FESEM, (b) TEM images, and (c) XRD pattern of the HKUST-1.

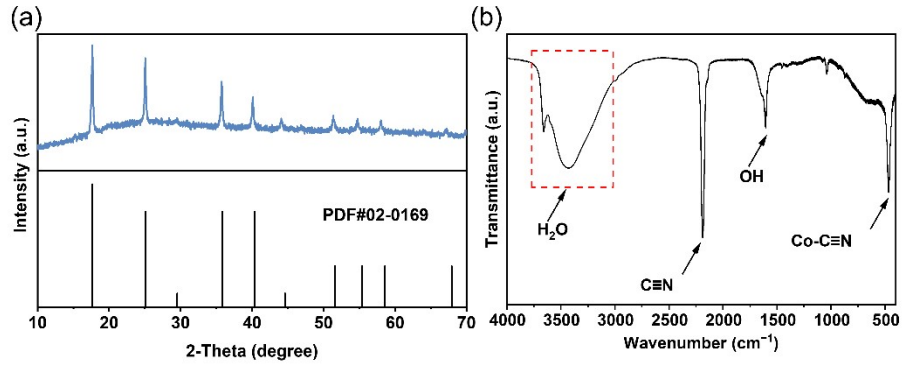

Fig. S2 (a) XRD patterns and (b) FT-IR spectra of the H-CuCo PBA.

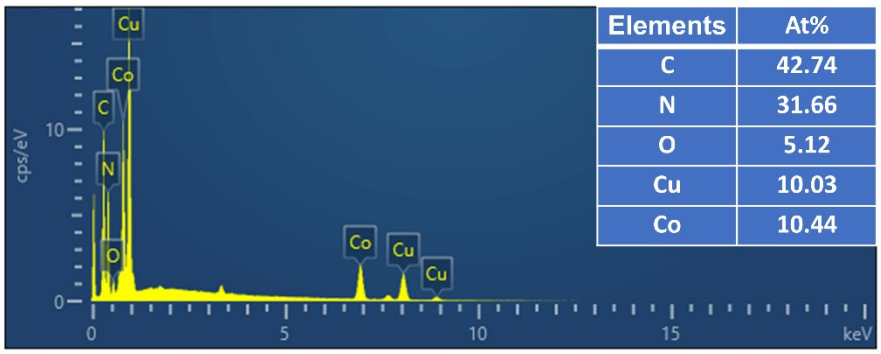

Elements	At%
C	42.74
N	31.66
O	5.12
Cu	10.03
Co	10.44

Fig. S3 EDS spectra of the H-CuCo PBA.

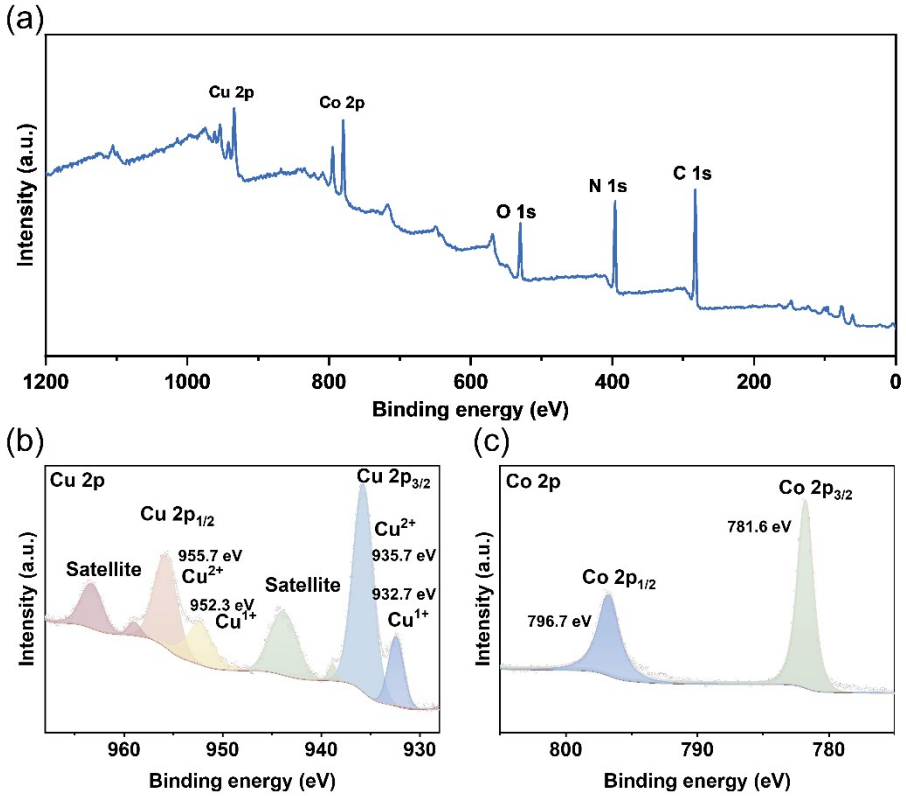

Fig. S4 (a) The XPS full spectrum of various elements of the H-CuCo PBA. (b) Cu 2p and (c) Co 2p high-resolution spectrum of the H-CuCo PBA.

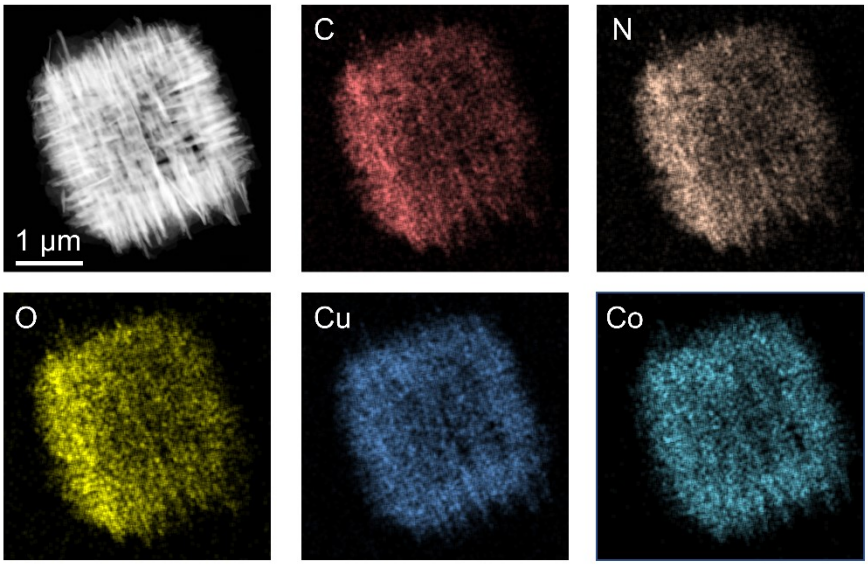

Fig. S5 STEM image and elemental mapping images of the H-CuCo PBA.

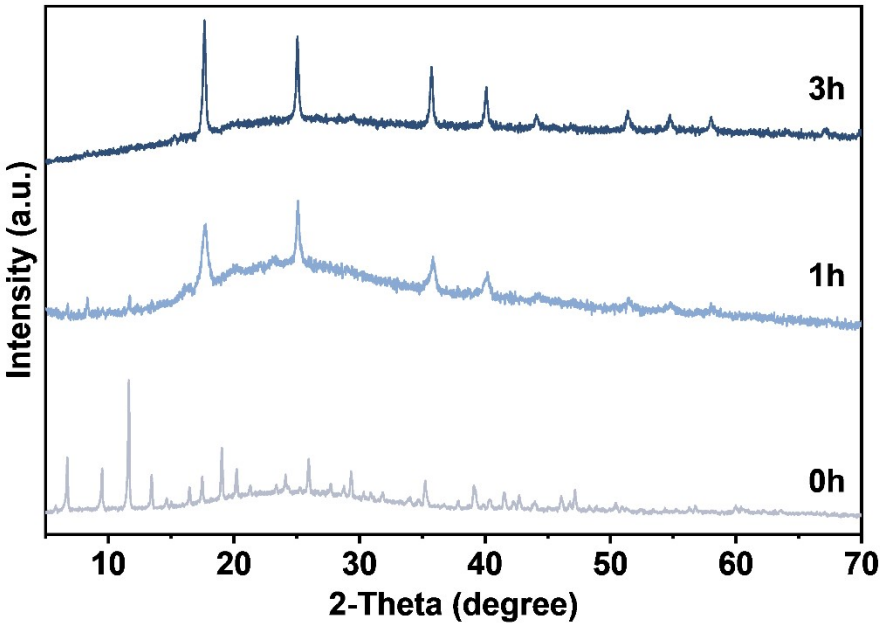

Fig. S6 XRD patterns of samples obtained at different reaction times of anion exchange: 0 h (HKUST-1), 1 h (coexistence of HKUST-1 and H-CuCo PBA), and 3 h (H-CuCo PBA).

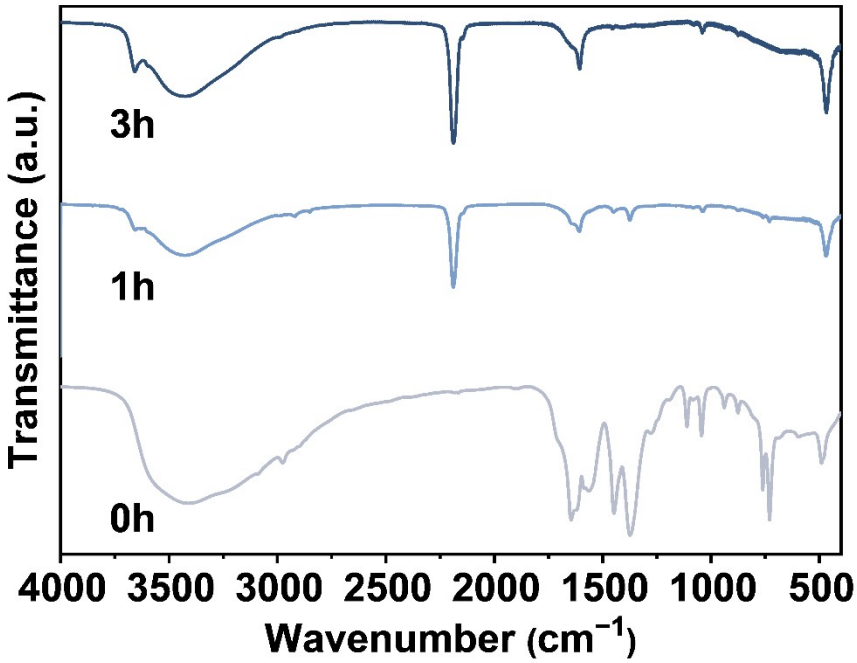

Fig. S7 FT-IR spectra of samples obtained at different reaction times of anion exchange: 0 h (HKUST-1), 1 h (coexistence of HKUST-1 and H-CuCo PBA), and 3 h (H-CuCo PBA).

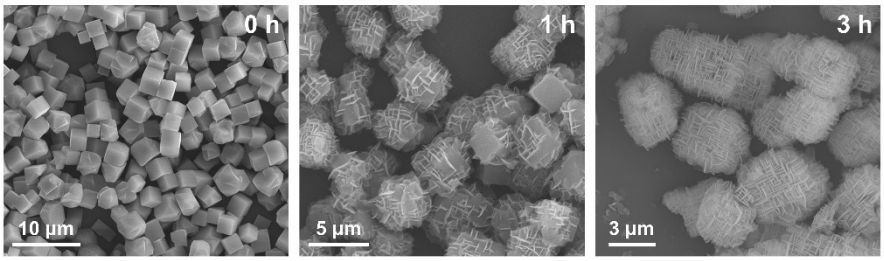

Fig. S8 FESEM images of samples obtained at different reaction times of anion exchange: 0 h (HKUST-1), 1 h (coexistence of HKUST-1 and H-CuCo PBA), and 3 h (H-CuCo PBA).

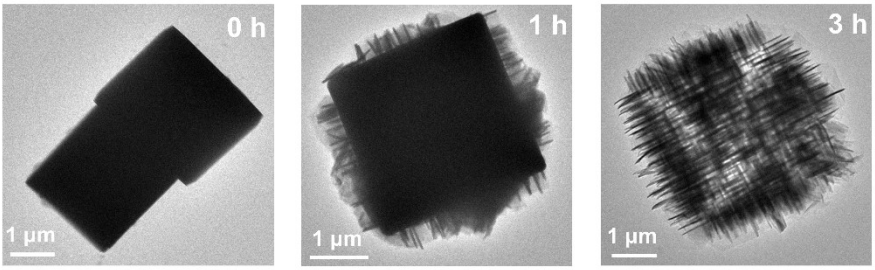

Fig. S9 TEM images of samples obtained at different reaction times of anion exchange: 0 h (HKUST-1), 1 h (coexistence of HKUST-1 and H-CuCo PBA), and 3 h (H-CuCo PBA).

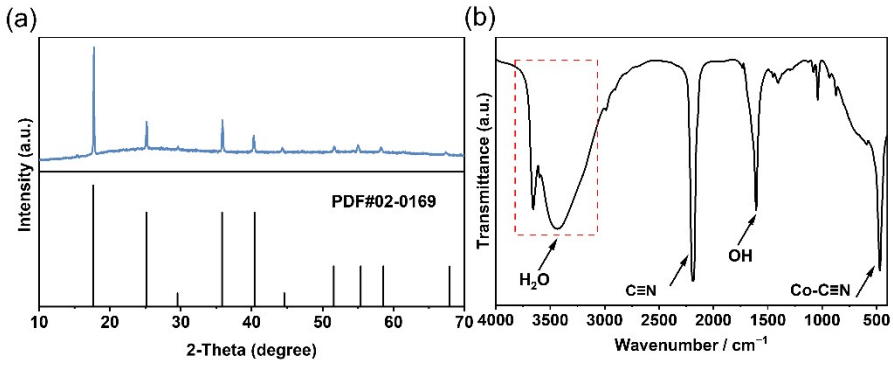

Fig. S10 (a) XRD patterns and (b) FT-IR spectra of the C-CuCo PBA.

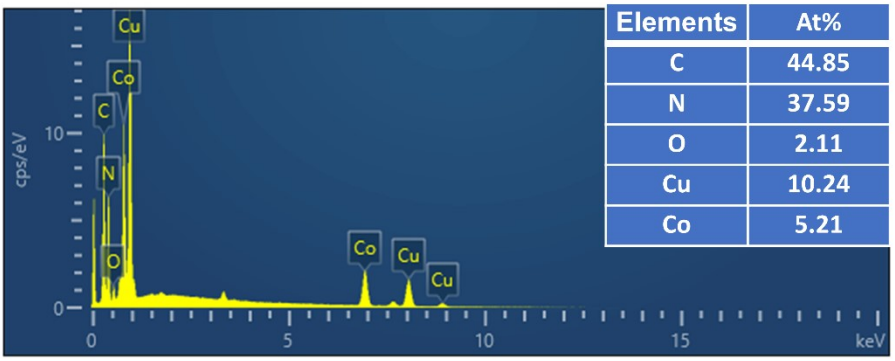

Elements	At%
C	44.85
N	37.59
O	2.11
Cu	10.24
Co	5.21

Fig. S11 EDS spectra of the C-CuCo PBA.

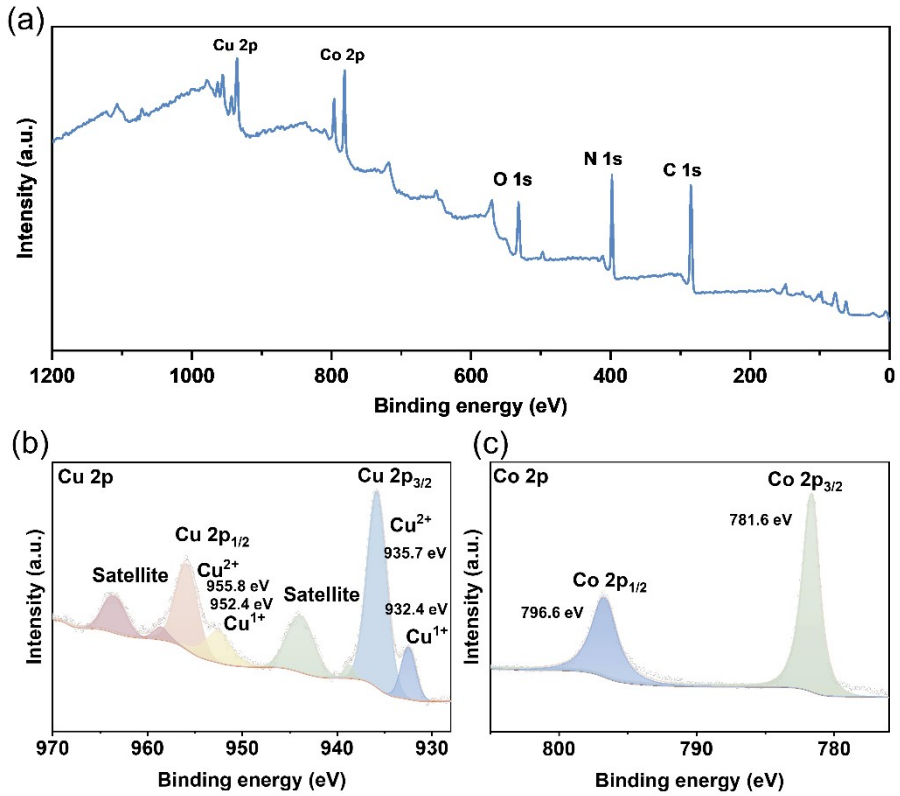

Fig. S12 (a) The XPS full spectrum of various elements of the C-CuCo PBA. (b) Cu 2p and (c) Co 2p high-resolution spectrum of the C-CuCo PBA.

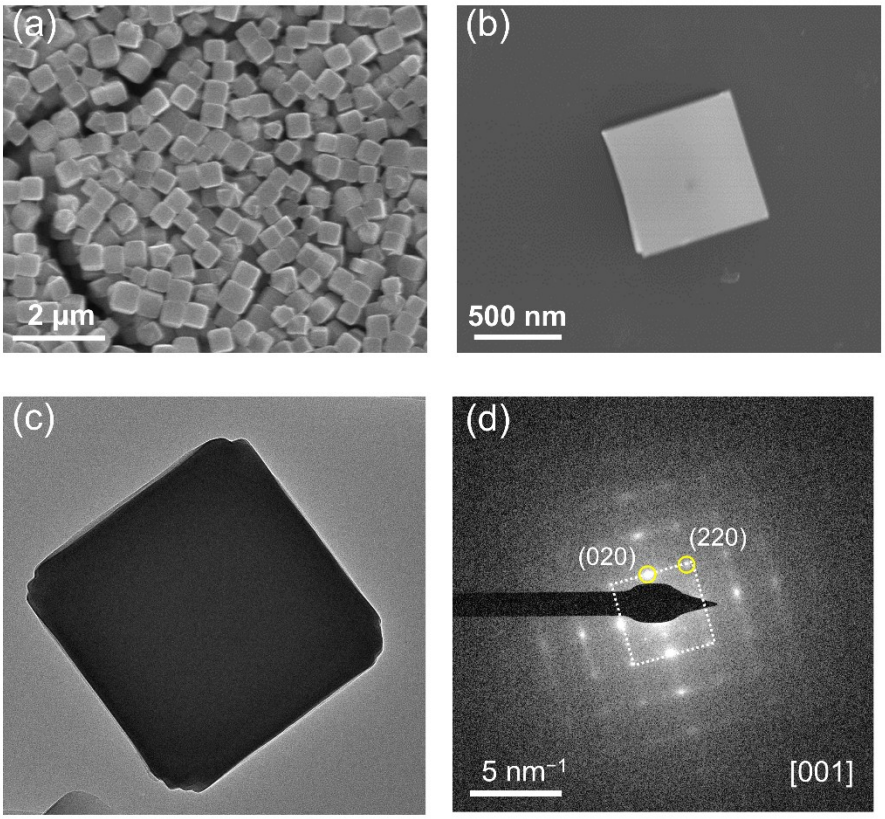

Fig. S13 (a-b) FESEM images, (c) TEM image, and (d) SAED pattern of the C-CuCo PBA.

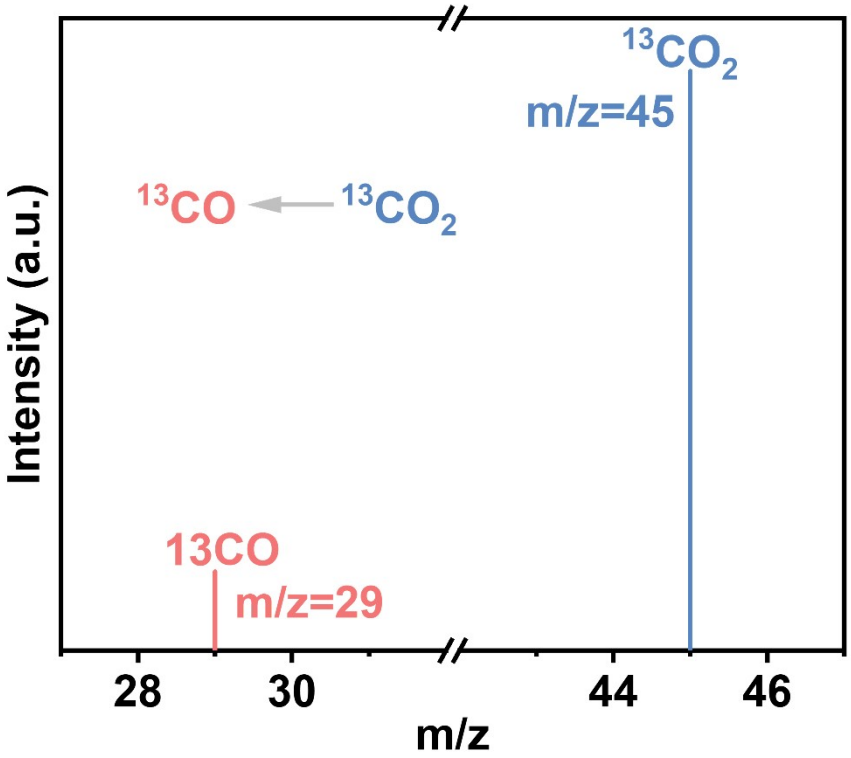

Fig. S14 Gas chromatography-mass spectrometry for ^{13}C isotope tracer tests.

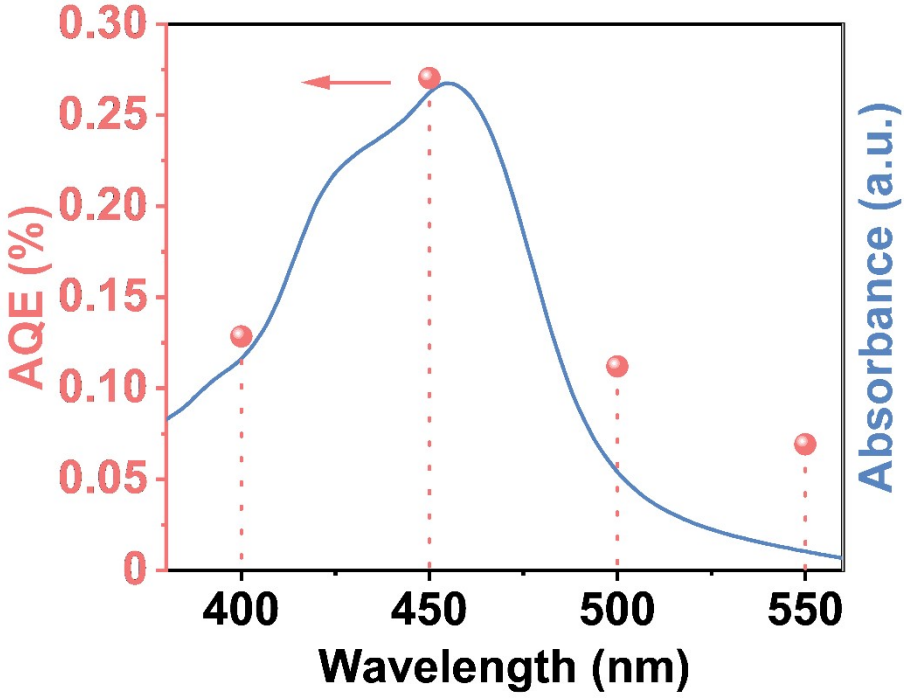

Fig. S15 AQE values of the H-CuCo PBA at several selected wavelengths and the UV-vis absorption spectrum of Ru-PS.

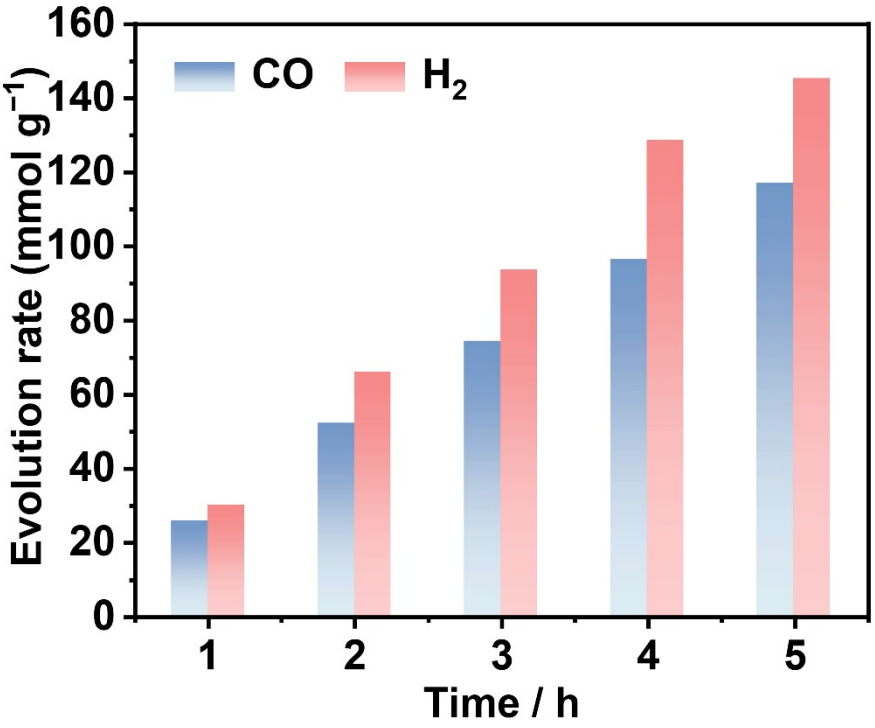

Fig. S16 Time-dependent CO/H_2 evolution rate over H-CuCo PBA.

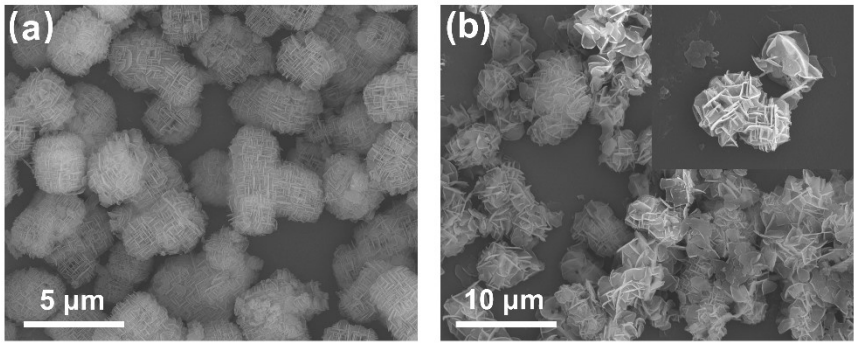

Fig. S17 The SEM images of the H-CuCo PBA before (a) and after (b) the cycling test.

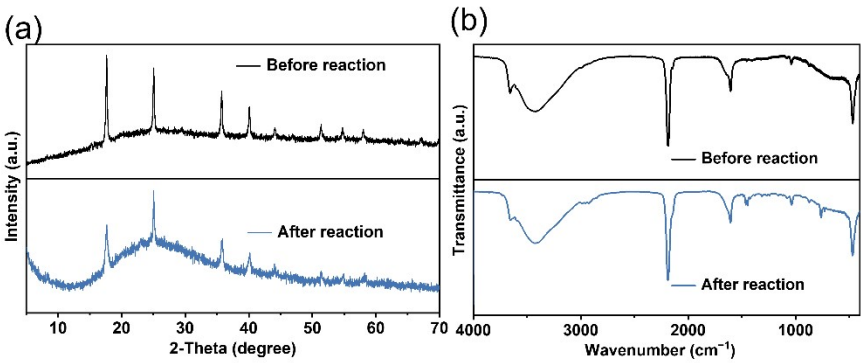

Fig. S18 (a) XRD patterns and (b) FT-IR spectra of the H-CuCo PBA before and after the cycling test.

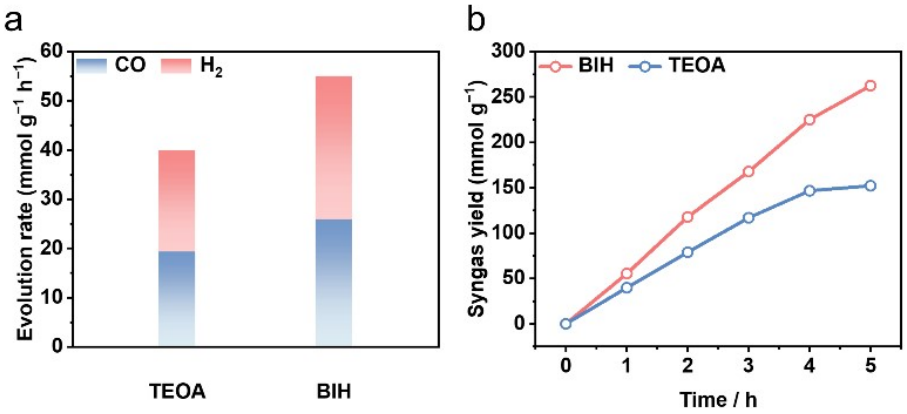

Fig. S19 (a) Comparison of CO/H_2 evolution rates of the H-CuCo PBA with TEOA and BIH; (b) Time-dependent syngas yield of the H-CuCo PBA with TEOA and BIH.

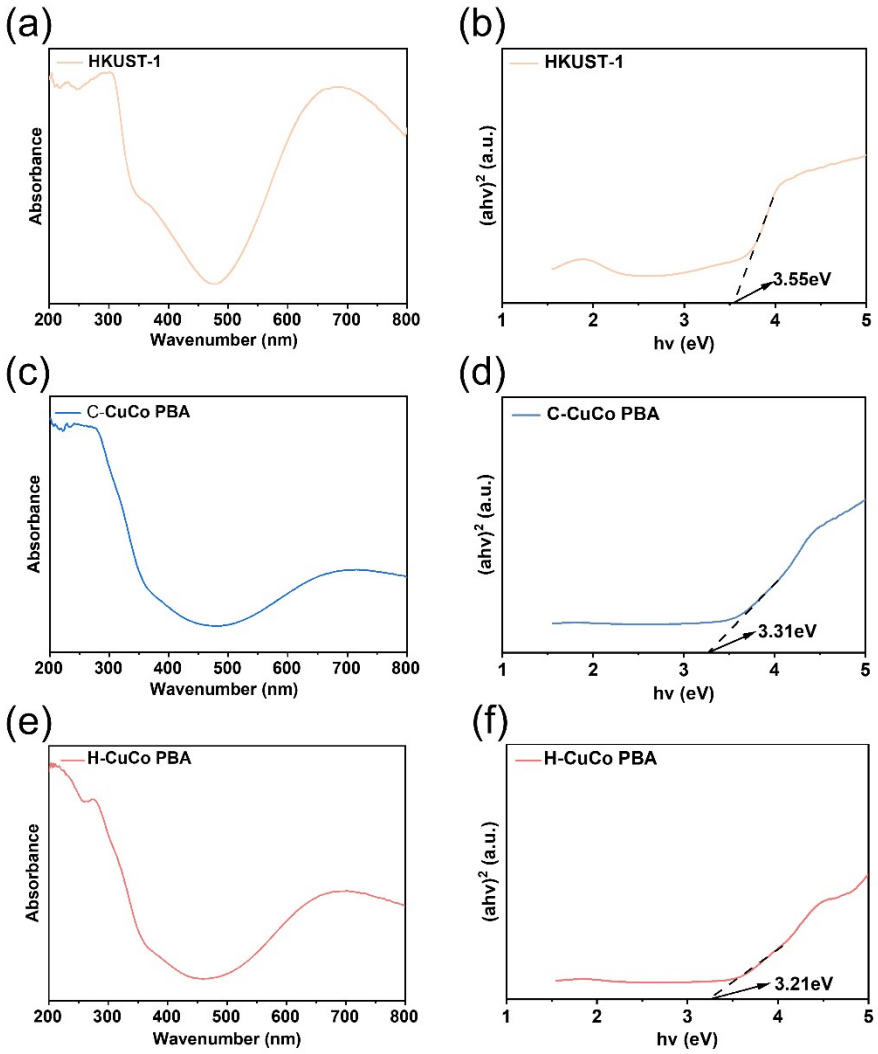

Fig. S20 UV-vis DRS and Tauc plots of all samples. HKUST-1 (a and b), C-CuCo PBA (c and d) and H-CuCo PBA (e and f).

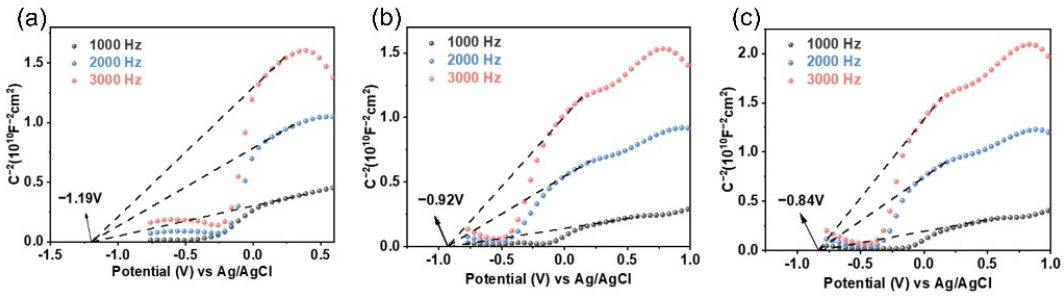

Fig. S21 Mott-Schottky plots of all samples. (a) HKUST-1, (b) C-CuCo PBA, (c) H-CuCo PBA.

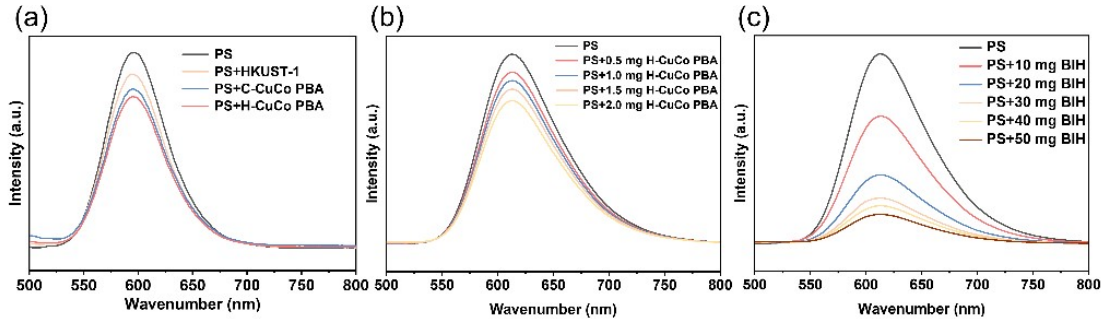

Fig. S22 (a) Steady-state PL spectra with different catalysts, (b) Steady-state PL spectra with different H-CuCo PBA contents, (c) Steady-state PL spectra with different BIH contents.

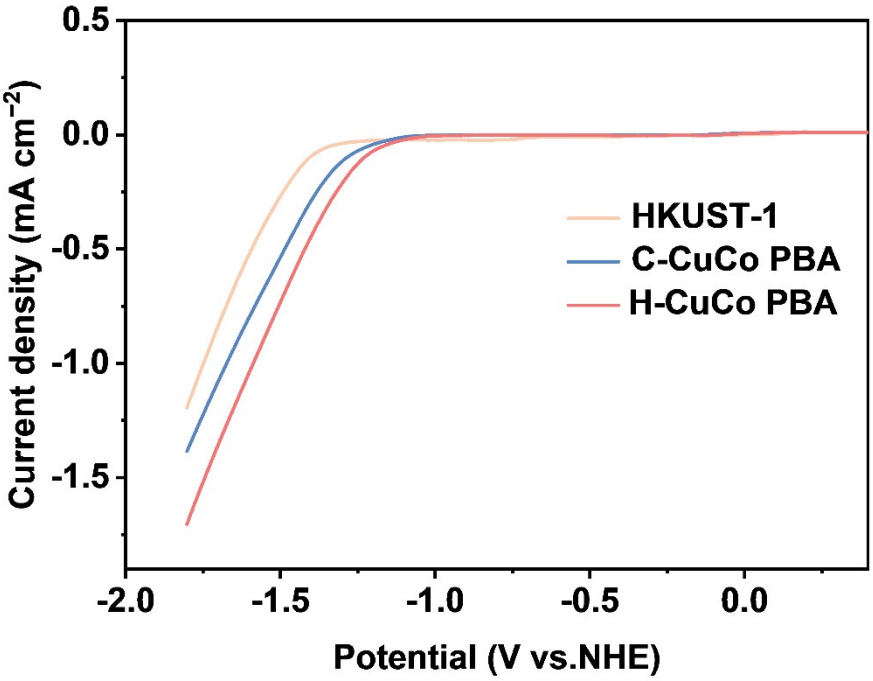

Fig. S23 LSV curves of the HKUST-1, C-CuCo PBA and H-CuCo PBA.

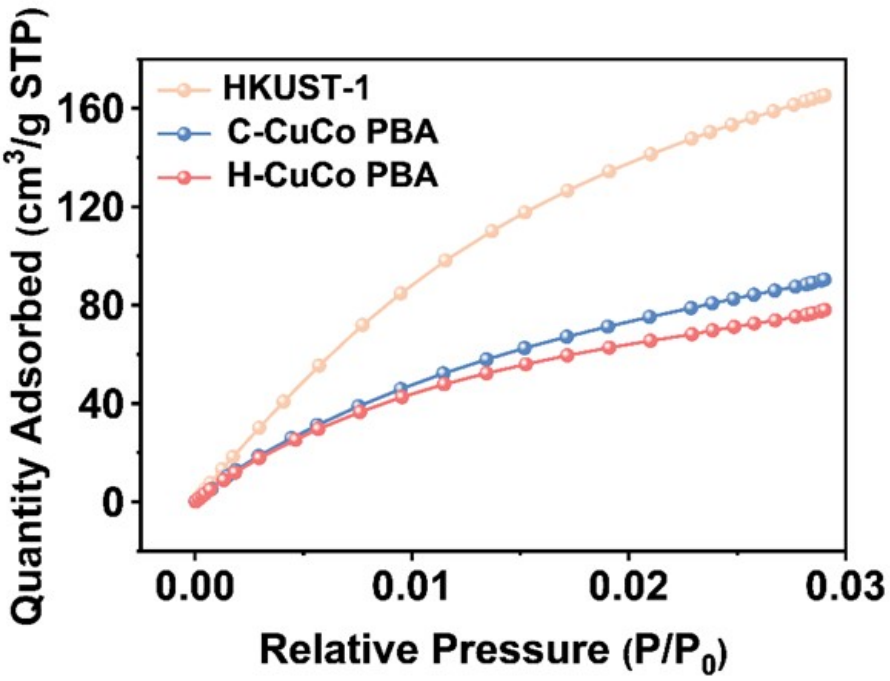

Fig. S24. CO_2 adsorption isotherms (at 273 K) of all samples.

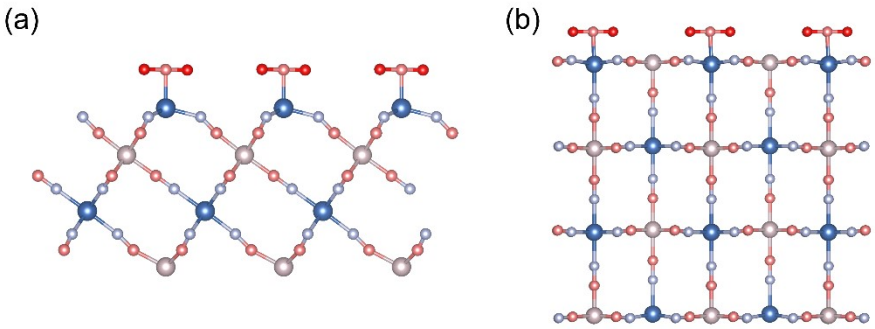

Fig. S25 Adsorption configurations of CO_2 on the Cu sites of the catalyst: (a) (111) facet, (b) (001) facet.

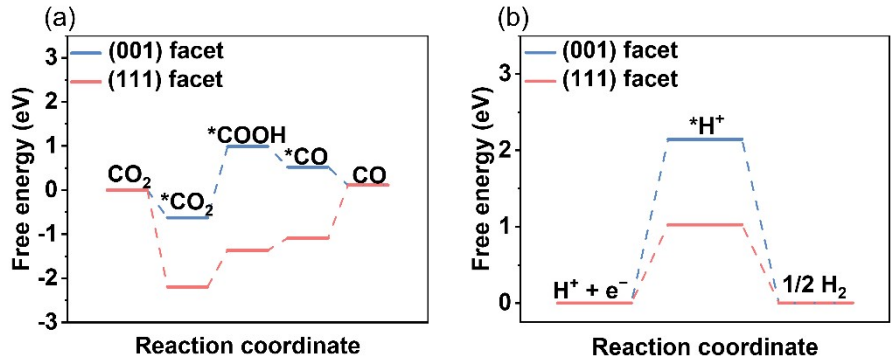

Fig. S26 Calculated free energy profiles for (a) CO_2-to-CO conversion and (b) HER on Co active sites of H-CuCo PBA with (111) and (001) facet exposure.

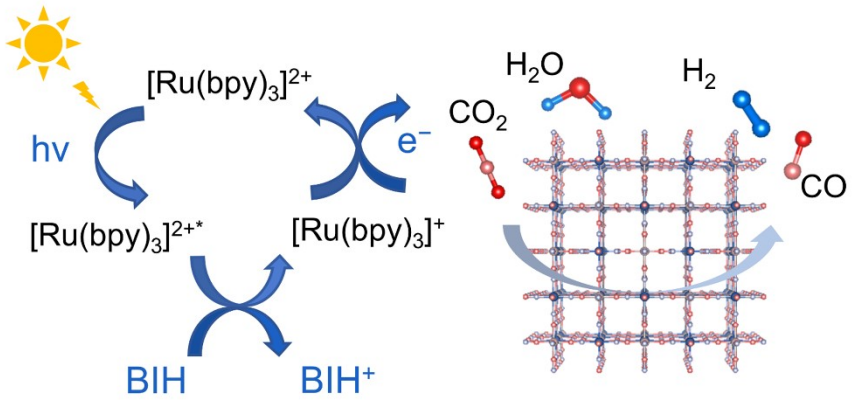

Fig. S27 Proposed mechanism for the photocatalytic reduction of CO_2 over H-CuCo PBA.

Table. S1 Performance comparison of H-CuCo PBA with other photocatalysts in terms of the Syngas yield.

Catalyst	Reaction medium	Syngas yield ($mmol\ g^{-1}h^{-1}$)	Reference
H-CuCo PBA	**$[Ru(bpy)_3]Cl_2 \cdot 6H_2O$, BIH**	**25.83 (CO) 29.15 (H_2)**	**This Work**
H-CuCo PBA	**$[Ru(bpy)_3]Cl_2 \cdot 6H_2O$, TEOA**	**19.24 (CO) 20.55 (H_2)**	**This Work**
ZIF-67	$[Ru(bpy)_3]Cl_2 \cdot 6H_2O$, TEOA	29.6 (CO) 10.29 (H_2)	Ref. 6
CoPc/Ni1-g-C3N4	$[Ru(bpy)_3]Cl_2 \cdot 6H_2O$, TEOA	2.14 (CO) 1.5 (H_2)	Ref. 7
COF-367-Co NSs	$[Ru(bpy)_3]Cl_2 \cdot 6H_2O$, Ascorbic Acid	2.52 (CO) 4.59 (H_2)	Ref. 8
TT-Por(Co)-COF	$[Ru(bpy)_3]Cl_2 \cdot 6H_2O$, TEOA	10.5 (CO) 8.94 (H_2)	Ref 9
30ZISCN	$[Ru(bpy)_3]Cl_2 \cdot 6H_2O$, TEOA	10.16 (CO) 3 (H_2)	Ref. 10
Co-TAPB-COF-1	$[Ru(bpy)_3]Cl_2 \cdot 6H_2O$, TEOA	8.39 (CO) 11.31 (H_2)	Ref. 11
Ce-$ZnIn_2S_4$	$[Ru(bpy)_3]Cl_2 \cdot 6H_2O$, TEOA	10 (CO) 9.8 (H_2)	Ref. 12
CIS/Co-PBA/NaY-5	$[Ru(bpy)_3]Cl_2 \cdot 6H_2O$, TEOA	0.31 (CO) 1.15 (H_2)	Ref. 13
B-BTO NF	$[Ru(bpy)_3]Cl_2 \cdot 6H_2O$, TEOA	5.49 (CO) 7.03 (H_2)	Ref. 14
Co@Si SACs	$[Ru(bpy)_3]Cl_2 \cdot 6H_2O$, TEOA	4.7 (CO) 4.4 (H_2)	Ref. 15
Co-2,3-DHTA-COF	$[Ru(bpy)_3]Cl_2 \cdot 6H_2O$, TEOA	5.64 (CO) 10.2 (H_2)	Ref. 16

References

1. Y. Wang, Y. Lü, W. Zhan, Z. Xie, Q. Kuang and L. Zheng, *J. Mater. Chem. A*, 2015, 3, 12796-12803.
2. G. Kresse and J. Furthmüller, *Comput. Mater. Sci.*, 1996, 6, 15-50.
3. P. E. Blöchl, *Physical review. B, Condensed matter*, 1994, 50, 17953-17979.
4. J. P. Perdew, J. A. Chevary, S. H. Vosko, K. A. Jackson, M. R. Pederson, D. J. Singh and C. Fiolhais, *Physical review. B, Condensed matter*, 1992, 46, 6671-6687.
5. D. J. Chadi and M. L. Cohen, *Phys. Rev. B*, 1973, 8, 5747-5753.
6. J. Qin, S. Wang and X. Wang, *Applied Catalysis B: Environmental*, 2017, 209, 476-482.
7. X. H. Liu, W. Xie, Y. Mao, M. Ce, Q. You, H. Yan, X. Zhang, G. I. N. Waterhouse and H. Huang, *Appl. Catal. B Environ. Energy*, 2026, 385, 126311.
8. W. Liu, X. Li, C. Wang, H. Pan, W. Liu, K. Wang, Q. Zeng, R. Wang and J. Jiang, *J. Am. Chem. Soc.*, 2019, 141, 17431-17440.
9. Y. Liu, W. K. Han, W. Chi, J. X. Fu, Y. Mao, X. Yan, J. X. Shao, Y. Jiang and Z. G. Gu, *Applied Catalysis B: Environmental*, 2023, 338, 123074.
10. Y. Liu, A. Deng, Y. Yin, J. Lin, Q. Li, Y. Sun, J. Zhang, S. Li, S. Yang, Y. Xu, H. He, S. Liu and S. Wang, *Appl. Catal. B Environ. Energy*, 2025, 362, 124724.
11. W. Zhou, X. Wang, W. Zhao, N. Lu, D. Cong, Z. Li, P. Han, G. Ren, L. Sun, C. Liu and W.-Q. Deng, *Nat. Commun.*, 2023, 14, 6971.
12. S. Sun, J. Guo, W. Zhang, Z. Wang, Y. Shi, M. Anpo and Y. Song, *Chem. Eng. Sci.*, 2026, 320, 122679.
13. G. Zhang, Z. Wang, D. Shi, G. Liu, T. He, J. Wu, J. Zhang and J. Wu, *Green Carbon*, 2025, 3, 11-21.
14. S. Xia, C. Wei, Y. Zhai, B. Ding, J. Yu and J. Yan, *Chem. Eng. J.*, 2023, 475, 146516.
15. H. Chen, Y. Xiong, J. Li, J. Abed, D. Wang, A. Pedrazo-Tardajos, Y. Cao, Y. Zhang, Y. Wang, M. Shakouri, Q. Xiao, Y. Hu, S. Bals, E. H. Sargent, C. Y. Su and Z. Yang, *Nat. Commun.*, 2023, 14, 1719.
16. Q. Zhang, S. Gao, Y. Guo, H. Wang, J. Wei, X. Su, H. Zhang, Z. Liu and J. Wang, *Nat. Commun.*, 2023, 14, 1147.